Tuning the Properties of N-Doped Biochar for Selective CO_2 Electroreduction to CO

Fu, Shilong; Li, Ming; de Jong, Wiebren; Kortlever, Ruud

Important note
To cite this publication, please use the final published version (if applicable).
Please check the document version above.

Tuning the Properties of N-Doped Biochar for Selective CO_2 Electroreduction to CO

Shilong Fu, Ming Li, Wiebren de Jong, and Ruud Kortlever*

ACCESS | ⅲⅼ Metrics & More | 🄴 Article Recommendations | 🆂🅸 Supporting Information

ABSTRACT: Nitrogen-doped (N-doped) carbon catalysts have been widely studied for electrochemical CO_2 reduction to CO. However, the correlation between the physicochemical properties of N-doped carbon catalysts and their electrocatalytic performance for the CO_2RR is still unclear. Herein, a series of N-doped biochar catalysts with different physicochemical properties were synthesized by tuning the carbonization temperature and N-doping level and used for the CO_2RR to analyze the structure−performance relationship. The prepared catalysts exhibited massive differences in maximum faradaic efficiency to CO from 26.8 to 94.9% at around −0.8 to −0.9 V vs RHE. In addition, we find that simply increasing the specific surface area and N-doping level of the catalysts does not effectively improve the catalytic performance for the CO_2RR. A multivariate correlation analysis reveals a negative correlation between the N-doping content and the electrochemical performance. The porous structural properties exhibit a positive correlation to the FE_{CO} but almost no correlation to j_{CO}. Interestingly, improving the degree of graphitization, surface hydrophobicity, the abundance of defects, and optimizing the porosity of the N-doped biochar catalyst can efficiently enhance the catalytic performance for the CO_2RR. We conclude that comprehensively analyzing the synergistic effect of various properties of N-doped biochar is critical to reveal structure−activity relationships.

KEYWORDS: CO_2 electrochemical reduction, N-doped carbon, carbon-based electrocatalysts, structure−performance correlation, electrocatalysis
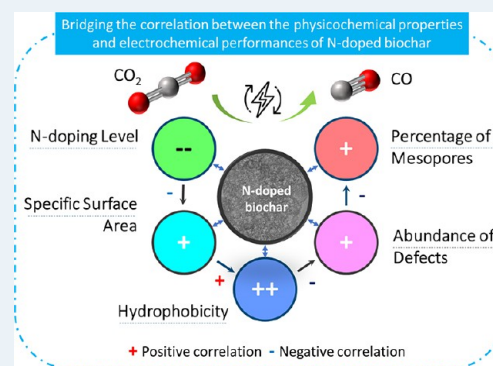
INTRODUCTION

Excessive CO_2 emissions have given rise to global warming and climate change.[1] In the past few decades, CO_2 conversion technologies have been developed to convert waste CO_2 into valuable products and close the anthropogenic carbon cycle.[2] Among them, the electrochemical CO_2 reduction reaction (CO_2RR) has attracted much attention,[3,4] as it can convert CO_2 into fuels and chemicals, simultaneously storing intermittent renewable electricity into chemical bonds.[5] Various reduction products such as CO, formic acid, methane, ethylene, and ethanol can be produced from the CO_2RR via different reaction pathways.[6,7] CO is an attractive product that can be widely used for downstream chemical transformations.[8] Moreover, the conversion of CO_2 to CO is a 2-electron transfer process that can be performed at relatively low overpotentials with high selectivity to CO.[9] Although the market price (per ton) of CO is lower than that of hydrocarbons, considering the power consumption and the cost of separation of multicarbon products, CO is still one of the most competitive products from the CO_2RR.[10] Au and Ag have been identified as effective electrocatalysts to reduce CO_2 to CO;[11] however, scarcity and a relatively high price can hinder the large-scale utilization of precious metal-based catalysts for the CO_2RR.

Recently, metal-free N-doped carbon materials have been shown as efficient alternative catalysts for the CO_2RR to CO.[12,13] Almost all advanced carbon materials, such as carbon nanotubes,[14] graphene,[15] and nanodiamonds[16] can be used as carbon precursors to synthesize N-doped carbon materials by in-situ doping or post-doping. Compared with Ag and Au-based electrodes, N-doped carbon materials exhibit a comparable catalytic performance but offer advantages, such as a relatively low cost, long stability, high tunability, and strong resistance to harsh reaction conditions.[17] However, the exact correlation between the physicochemical properties of N-doped carbon materials and their electrochemical performance for the CO_2RR is still unclear. Generally, the specific surface area and N-doping content are considered as two important factors governing catalytic performance, with many studies attributing better catalytic performances to an increase in either the specific surface area or N-doping levels.[18,19] The

ACS Publications

© 2023 The Authors. Published by
American Chemical Society

10309

https://doi.org/10.1021/acscatal.3c01773
ACS Catal. 2023, 13, 10309−10323

rationale behind this is that a larger specific area and rich pore structure enhances the mass transfer of reactants and electrolytes,[20] while the introduction of N into the carbon skeleton tunes the atomic charge and spin distribution of carbon materials and acts as an active site for the CO_2RR.[21] Although the exact nature of the active site of N-doped carbon materials is still under debate, the catalytic performance for the CO_2RR has been enhanced by increasing either the total N-doping content or the content of specific N-containing species, as verified by theoretical calculations and experimental analyses.[22−27]

Interestingly, there are some studies that do not fully support the relationship between the electrocatalytic performance and the specific surface area and N-doping content. For instance, Daiyan et al.[28] gradually reduced the N content by an annealing treatment and found that a lower N content leads to better performances, ultimately linking the catalytic performance to the abundance of defects. Furthermore, Hursán et al.[29] prepared N-doped carbon catalysts with different pore sizes via a sacrificial support method and found that the catalysts showed different selectivity, activity, and stability even with similar N-doping content and a similar distribution of N-containing species and no correlation was found between the specific surface area and catalytic performance. In previous work, we also found that there is no significant correlation between the catalytic performance and specific surface area, and N-doping content and that the ratio of mesopores and the degree of graphitization play an essential role.[30] We believe that an over-emphasis on the effects of specific surface area and N-doping level can easily lead to lopsided conclusions, which do not fully reflect the actual structure−performance relationships of N-doped carbon catalysts. Therefore, to develop better N-doped carbon catalysts for the CO_2RR, it is necessary to further elucidate the structure−performance relationship of N-doped carbon materials through a comprehensive and integrated analysis.

Biomass can be used as a carbon precursor to synthesize N-doped carbon materials for the CO_2RR. Compared to fossil-derived carbon materials, biochar is a renewable source, and the raw materials are generally widely distributed, abundantly available, easily accessible, and more eco-friendly.[31] In addition, using biochar to synthesize N-doped carbon materials can provide sustainable and "green" catalysts for the CO_2RR, simultaneously enhancing the added value of waste biomass and providing a possibility to realize a high-value application of waste biomass materials.[32] More importantly, the lignocellulose-derived biochar catalysts have good textural tunability. By changing different preparation conditions, such as the carbonization temperature, N-doping precursor and doping amount, and the type and amount of activator, one can easily obtain carbon materials with significantly different physicochemical properties. Therefore, testing biomass-derived N-doped carbon materials with different properties for the CO_2RR can help in investigating the correlation between different physicochemical properties of catalysts and their catalytic performance.

In this study, a set of sugarcane bagasse-derived N-doped carbon catalysts were synthesized by a one-step pyrolysis method. The physicochemical properties of the N-doped biochar catalysts were tuned by changing the carbonization temperature and N-doping level, respectively. Combining the characterization results and the electrochemical measurements, we have conducted a comprehensive analysis of the influence of the physicochemical properties of N-doped biochar materials on their CO_2RR performance. A higher carbonization temperature (800 °C) yielded an optimal N-doped biochar, which showed an 89.3% faradaic efficiency to CO at −0.82 V vs RHE. Interestingly, we find that simply increasing the amount of N-doping is not an efficient method to improve the CO_2RR performance of the catalysts. Moreover, we perform a multivariate correlation analysis by a statistical approach to analyze the correlation between physicochemical properties and electrochemical performance. The N-doping content shows a negative correlation to the CO_2RR performance, whereas the surface hydrophobicity shows a strong positive correlation. Additionally, the porous structural properties (specific surface area, pore volume, etc.) exhibit a positive correlation to the FE_{CO} but almost no correlation to the j_{CO}. Our results show that the CO_2RR performance can be enhanced by improving the hydrophobicity and abundance of defects and optimizing the porosity distribution of N-doped biochar catalysts. These insights can provide guidance for the design and analysis of efficient N-doped carbon catalysts for CO_2RR.

■ EXPERIMENTAL SECTION

All chemicals were used as received without further purification. The urea (CN_2H_4O, ≥99%), sodium hydroxide (NaOH, ≥98%), potassium bicarbonate ($KHCO_3$, ≥99.95%, trace metal basis), and Nafion resin solution (5 wt % in lower aliphatic alcohol and 15−20% water) were purchased from Sigma-Aldrich. The hydrochloric acid (HCl, 37%) and isopropanol (C_3H_8O, ≥99.5%) were purchased from VWR International. 0.1 M $KHCO_3$ electrolyte solutions and 1 M HCl solutions were prepared from ultrapure water (Milli-Q IQ 7000, 18.2 MΩ). ICP-OES analyses of the freshly prepared and used 0.1 M $KHCO_3$ electrolytes indicated that the concentration of transition metal is below the limit of detection, preventing the spontaneous formation of M-N_x sites on the N-doped carbon catalysts.

Synthesis of Catalysts. Activated N-doped biochar (ANBC) samples were synthesized by a one-step pyrolysis method. In brief, the received sugarcane bagasse (Maharashtra, India) was washed with ultrapure water three times to remove dust and gravel from the surface and dried in an oven (105 °C) overnight. The dried sugarcane bagasse was ground and sieved to obtain particle sizes of less than 425 μm before use. Afterward, 5 g of sugarcane bagasse powder, 10 g of urea, and 15 g of NaOH (mass ratio = 1:2:3) were added into a crucible and stirred for 30 min to make a homogeneous mixture. Then, the mixture was transferred into a muffle furnace, which was purged with N_2 with a flow rate of 100 mL/min for 1 h. The carbonization was carried out at the desired final temperature (600, 700, 800, or 900 °C) for 1 h with a ramping rate of 10 °C/min under a N_2 atmosphere (100 mL/min, 99.99%, Linde gas). After cooling down to ambient temperature, the obtained product was washed with 1 M HCl for 4 h at 60 °C to remove the residual sodium-containing salts and other impurities. Afterward, the black powder was filtered and rinsed thoroughly with ultrapure water until it reached a neutral pH. Finally, the activated N-doped biochar catalyst was collected and dried at 105 °C for 12 h. The obtained catalysts are designated as ANBCT, where T represents the carbonization temperature.

To investigate the effect of the N-doping level on the performance of the ANBC for the CO_2RR, a series of catalysts with different N-doping levels (ANBC800-XN) were synthe-
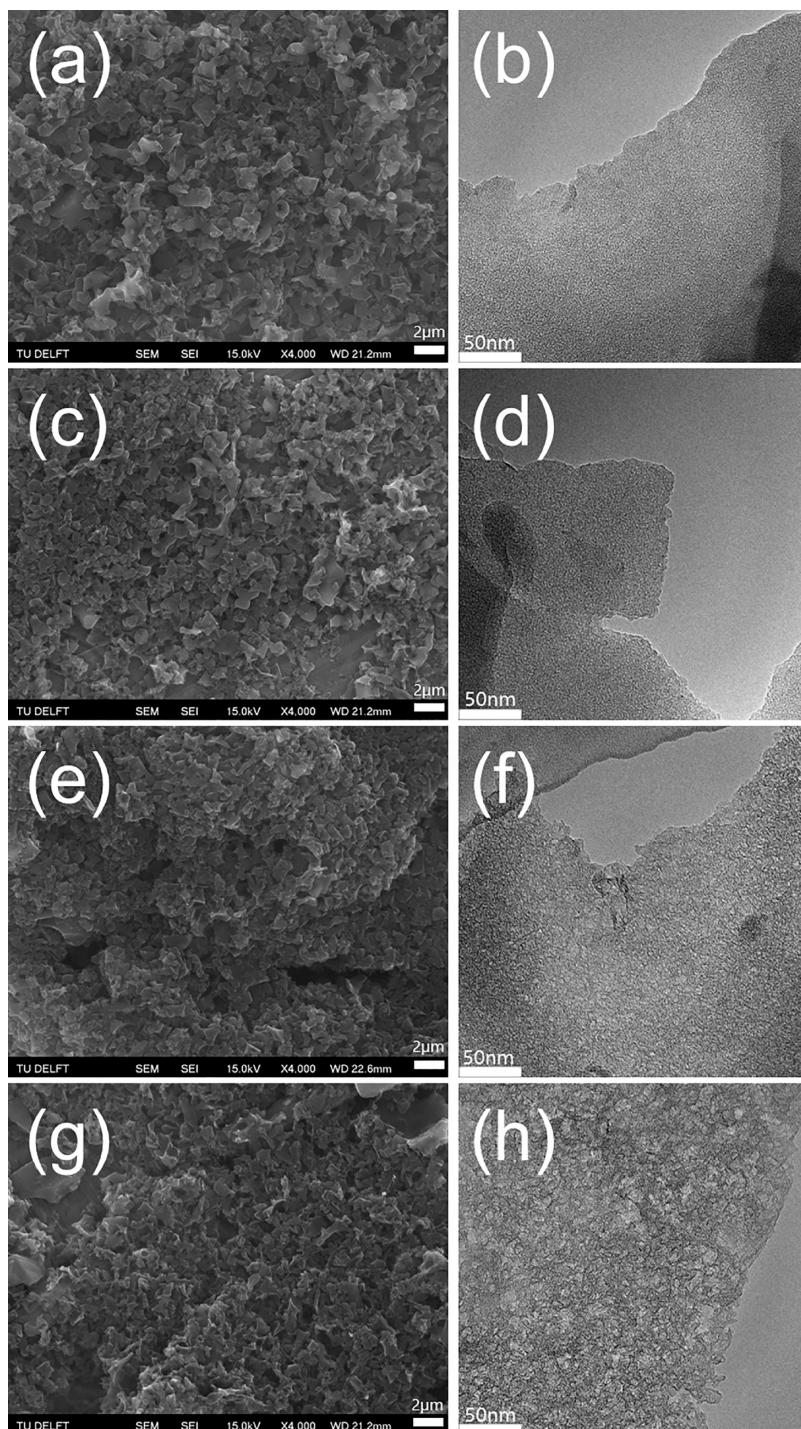
Figure 1. SEM (left) and TEM (right) images of ANBC600: (a), (b); ANBC700: (c), (d); ANBC800: (e), (f); and ANBC900: (g), (h).

sized using the same pyrolysis method at 800 °C while changing the ratio of urea. ANBC800-SN (ANBC800 doped with a slight amount of nitrogen) was synthesized with the mass ratio of sugarcane bagasse, urea, and NaOH being 1:0.5:3, ANBC800-LN (ANBC800 doped with a low amount of nitrogen) was synthesized with a ratio of 1:1:3, and ANBC800-HN (ANBC800 doped with a high amount of nitrogen) was synthesized with a ratio of 1:3:3, respectively. The specific formulation and carbon yields of all prepared samples are listed in Table S1.

Catalyst Characterization. The morphology and microstructures of all samples were visualized by using a JEOL JSM-6500F scanning electron microscope (SEM) and a JEOL JEM1400 transmission electron microscope (TEM). The porosity characteristics of all carbon catalysts were measured by isothermal N_2 adsorption−desorption at 77 K using a Micromeritics TriStar II 3020 instrument. Specific surface areas were determined by the Brunauer−Emmett−Teller (BET) method, and pore size distributions were calculated based on a density function theory (DFT) model. X-ray diffraction (XRD) patterns were obtained using a Bruker AXS
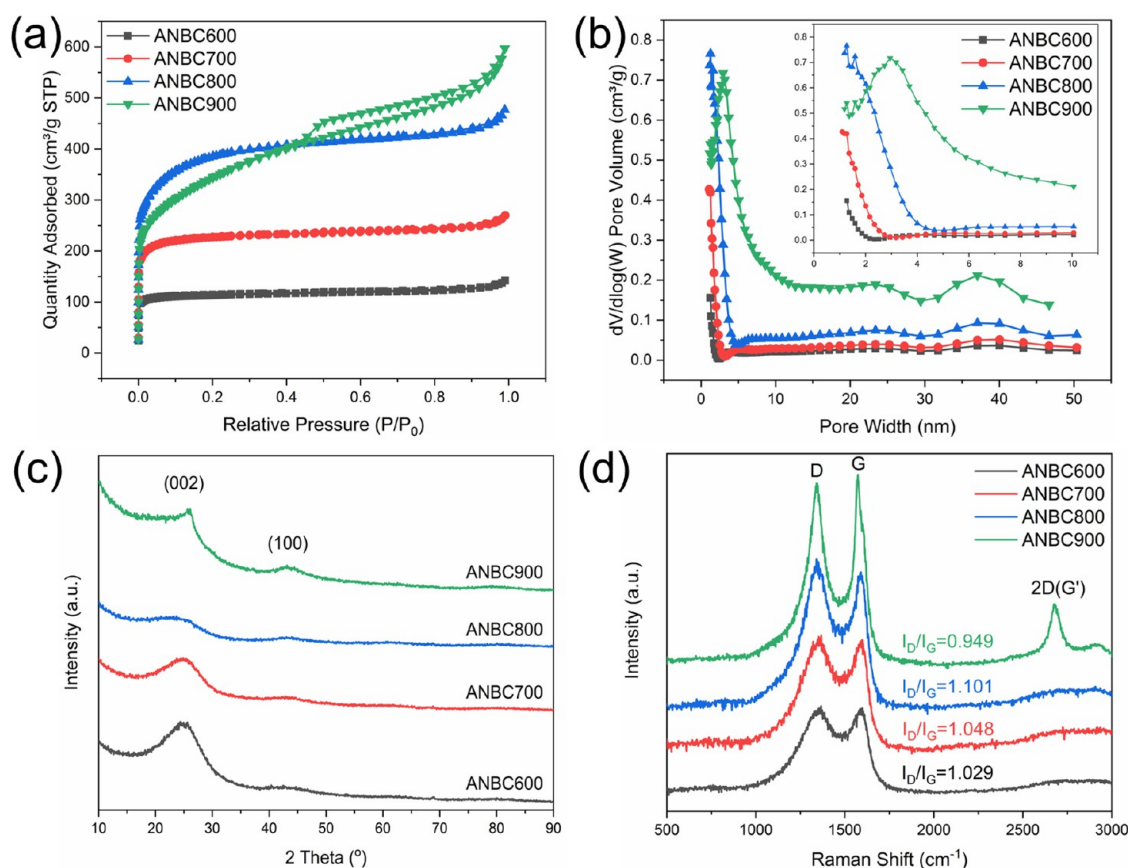
Figure 2. (a) N$_2$ adsorption−desorption isotherms; (b) pore size distribution; (c) XRD patterns; and (d) Raman spectra of the ANBCT samples with different carbonization temperatures.

D2 Phaser with Cu Kα radiation (λ = 0.15406 nm). Raman spectra were recorded from 500 to 3000 cm^{-1} on a Horiba Scientific LabRAM HR Evolution Raman Spectroscopy system with an excitation wavelength of 514 nm. X-ray photoelectron spectroscopy (XPS) measurements were carried out on a Thermo Scientific Kα system with Al Kα radiation (1486.7 eV). All binding energies for XPS spectra were calibrated according to the C 1s peak at 284.8 eV in CasaXPS. Contact angle measurements were performed via sessile drop using an OCA 25 goniometer (Dataphysics instruments Gmbh, Filderstadt, Germany), and 2 μL of droplets were dispensed onto substrates using an automatic pipetting unit. Measurements were taken in ambient air with a temperature in the range of 20−24 °C.

Electrode Preparation. To prepare a working electrode, 4 mg of catalyst powder was dispersed in a solvent mixture containing 800 μL of ultrapure water, 150 μL of isopropanol, and 50 μL of 5% Nafion perfluorinated resin solution (5 wt % in lower aliphatic alcohols and 15−20% water) under sonication for 1 h to obtain a homogeneous ink. Afterward, 200 μL of the catalyst ink was drop-casted on the center of a 25 mm × 25 mm glassy carbon plate (HTW Hochtemperatur-Werkstoffe GmbH, Germany) and dried at room temperature. The geometric surface area of the working electrode exposed to the electrolyte was equal to 1 cm^2, and the catalyst loading was equal to 0.8 mg/cm^2.

A 25 mm × 25 mm × 0.1 mm platinum foil (99.9%, Mateck, Germany) was used as a counter electrode. The counter electrode was cleaned by flame annealing 3 times to remove any possible impurities before use. A leak-free Ag/AgCl

electrode (40 mm length, Innovative instrument) was used as a reference electrode. The reference electrode was checked every time before use by comparing it with a master Ag/AgCl reference electrode (BASi, MF-2056), which is never used experimentally and is kept in pristine working condition.

Electrochemical Measurements. Electrochemical measurements of different catalysts were performed in a gas-tight two-compartment H-cell at ambient conditions. Each compartment contained 1.8 mL of 0.1 M KHCO$_3$ electrolyte, with the anode and cathode compartment separated by a Selemion AMV anion exchange membrane (AGC group, Japan).[33] Before electrolysis, the electrolyte was purged with CO$_2$ for at least 15 min to saturate the 0.1 M KHCO$_3$ electrolyte. A Biologic SP-200 potentiostat (Biologic, France) was used to control the potential and measure the resulting currents. All potentials in this study are converted to the reversible hydrogen electrode (RHE) scale according to the formula: E (V vs RHE) = E (V vs Ag/AgCl) + 0.197 + 0.059 × pH. Linear sweep voltammograms (LSV) were recorded in Ar-saturated (pH = 8.3) and CO$_2$-saturated (pH = 6.8) 0.1 M KHCO$_3$ electrolytes at a scan rate of 5 mV/s. The electrochemically active surface areas (ECSA) of the electrodes were determined by measuring the double layer capacitance (C_{dl}), which was derived from cyclic voltammetry measurements with a scan rate at 5, 10, 25, and 50 mV/s in a potential window from 0.45 to 0.55 V vs RHE. The C_{dl} was estimated by plotting the $\triangle j$ ($j_a - j_c$)/2 at 0.50 V vs RHE against the scan rates, where the slope of the plot gives the C_{dl}. Chronoamperometric electrolysis measurements were conducted for 7 different potentials from −0.5 to −1.1 V vs RHE (with iR

compensation), and each potential was applied for 1 h. The cell resistance (R_u) was measured by potentiostatic electrochemical impedance spectroscopy (PEIS). Automatic ohmic drop correction was corrected for 85% of R_u during CO_2RR measurements, while the remaining 15% was corrected manually afterward. During the chronoamperometry tests, CO_2 was purged continuously into the catholyte with a flow rate of 8 mL/min through a mass flow controller (EL-FLOW Select, Bronkhorst). The gaseous products from the catholyte compartment were measured every 2 min by an in-line gas chromatograph (Compact GC 4.0, G.A.S). The GC was equipped with a flame ionization detector (FID) to measure the hydrocarbon compounds and two thermal conductivity detectors (TCD) to measure CO and H_2, respectively. A standard calibration curve was made using custom gas mixture cylinders with known concentrations of product gasses in CO_2 (Linde gas Benelux B.V.). An aliquot of the catholyte was collected at the end of the measurements, and liquid-phase products were quantified using high-performance liquid chromatography (HPLC, Agilent 1260 Infinity). Then, 5 μL of the liquid sample was injected into two Aminex HPX 87-H columns (Bio-rad) placed in series. The column oven temperature was maintained constant at 60 °C, with a steady flow rate of 0.6 mL/min of an aqueous 1 mM H_2SO_4 eluent, and a refractive index detector (RID) was used for product detection. The total current density and the faradaic efficiency of gaseous products for each sample are average values that were collected from the reaction interval between 42 and 54 min, where a relatively stable CO_2RR performance is obtained.

■ RESULTS AND DISCUSSION

Effect of Carbonization Temperature. SEM and TEM measurements were performed to visualize the morphology of the activated N-doped biochar (ANBCT) samples prepared at different temperatures (see Figure 1). As the carbonization temperature increased from 600 to 900 °C, similar morphological structures were observed with SEM, which displayed an intertwined particle-stacked structure with multilevel channels. SEM-EDS measurements confirmed that N heteroatoms were doped uniformly into the carbon framework (see Figure S1). To further study the microstructure of the prepared samples, TEM measurements were carried out. As shown in Figure 1b,d, numerous micropores can be observed in the catalysts prepared at 600 and 700 °C. At higher carbonization temperatures, mesopores and wrinkled nanotextures were generated and can be observed clearly in the catalysts prepared at 800 and 900 °C.

To further evaluate the porosity of the ANBCT catalysts, N_2 adsorption−desorption isothermal analyses were executed. As shown in Figure 2a, the isotherms of ANBC600, ANBC700, and ANBC800 can be categorized into a combined type I and type IV isotherm according to the IUPAC classification. The isotherm increased rapidly at low relative pressure ($P/P_0 < 0.05$) and then remained almost constant. A small hysteresis loop can be observed in these isotherms, which indicates that a small amount of mesopores were developed in these samples. In addition, the small upturned tail observed at a high relative pressure ($P/P_0 > 0.95$) indicates that macropores retain in these samples. The isotherm of ANBC900 can be classified as type IV. An apparent H4 hysteresis loop in the relative pressure ranging from 0.45 to 0.95 suggests the existence of mesopores, which agrees well with the TEM images. The pore size distribution of ANBCT samples calculated by a density

functional theory (DFT) model is shown in Figure 2b. The pore structural properties are summarized in Table S2. Overall, with an increase in carbonization temperature, the ANBC samples exhibit a broader pore size distribution. Moreover, the specific surface area increases from 450.5 m²/g for ANBC600 to 1426.9 m²/g for ANBC800 with the increase of carbonization temperature from 600 to 800 °C. As the carbonization temperature increased further to 900 °C, the specific surface area of ANBC900 decreased slightly to 1228.7 m²/g. However, the total pore volume kept increasing with rising carbonization temperatures. The increase in the specific surface area and total pore volume is explained by a more efficient reaction of the activator (NaOH) with the bagasse and urea with increasing carbonization temperatures.[34] When the carbonization temperature is increased to 900 °C, the extreme temperature damages the structure, and part of the micropores collapse or merge into mesopores.[35] This leads to a decrease in the specific surface area but an increase in the total pore volume. Therefore, the ratio of mesopores (56.3%) and the average pore size (2.7 nm) of ANBC900 are larger than for other samples (Table S2), which is consistent with the TEM results. In summary, these results indicate that the carbonization temperature plays a vital role in the porosity development of the ANBC samples.

The XRD patterns of the ANBCT samples are plotted in Figure 2c. All of the ANBCT samples show two broad diffraction peaks located at around $2\theta = 25$ and 44°, which are ascribed to the (002) and (100) planes of graphite, showing as dominant features of amorphous carbon.[36] Notably, the (002) peak reflection of ANBC900 shifts slightly to around 26°, indicating a higher degree of graphitization than other samples.[37] The Raman spectra in Figure 2d show two intensive peaks centered at around 1350 and 1590 cm⁻¹ that are attributed to the D band and G band of carbon materials. In particular, ANBC900 shows another distinct peak at 2700 cm⁻¹, which is considered as a typical signal of a graphite/graphene structure,[38] indicating that ANBC900 has a higher degree of graphitization. The relative intensity ratio of the D and G bands (I_D/I_G) is used as an index to evaluate the abundance of defects of carbon materials, with higher I_D/I_G values indicating a larger amount of defects.[39] The I_D/I_G values of ANBCT samples show a slowly increasing trend from 1.029 (ANBC600) to 1.101 (ANBC800) and then a slight decrease to 0.949 as the temperature rises to 900 °C. This suggests that the activator and nitrogen precursor create more defects in the carbon structure from 600 to 800 °C. However, the extremely high temperature (900 °C) also promotes structural alignment by removing heteroatoms, thus increasing the degree of graphitization.[40] Therefore, the carbonization temperature leads to a trade-off between the abundance of defects and the degree of graphitization.

X-ray photoelectron spectroscopy (XPS) was used to verify the surface chemical composition of the ANBCT samples.[41] In the XPS survey scan spectra (Figure S2), three obvious peaks located at around 285.1, 400.1, and 533.3 eV are observed that are ascribed to C 1s, N 1s, and O 1s, respectively. The surface atomic element concentrations are summarized in Table S3. With the carbonization temperature increasing from 600 to 900 °C, the surface concentrations of N and O are gradually reduced; however, the atomic concentration of C gradually increases from 82.5 at % (ANBC600) to 92.7 at % (ANBC900). This indicates that the higher carbonization temperature can effectively increase the degree of graphitiza-
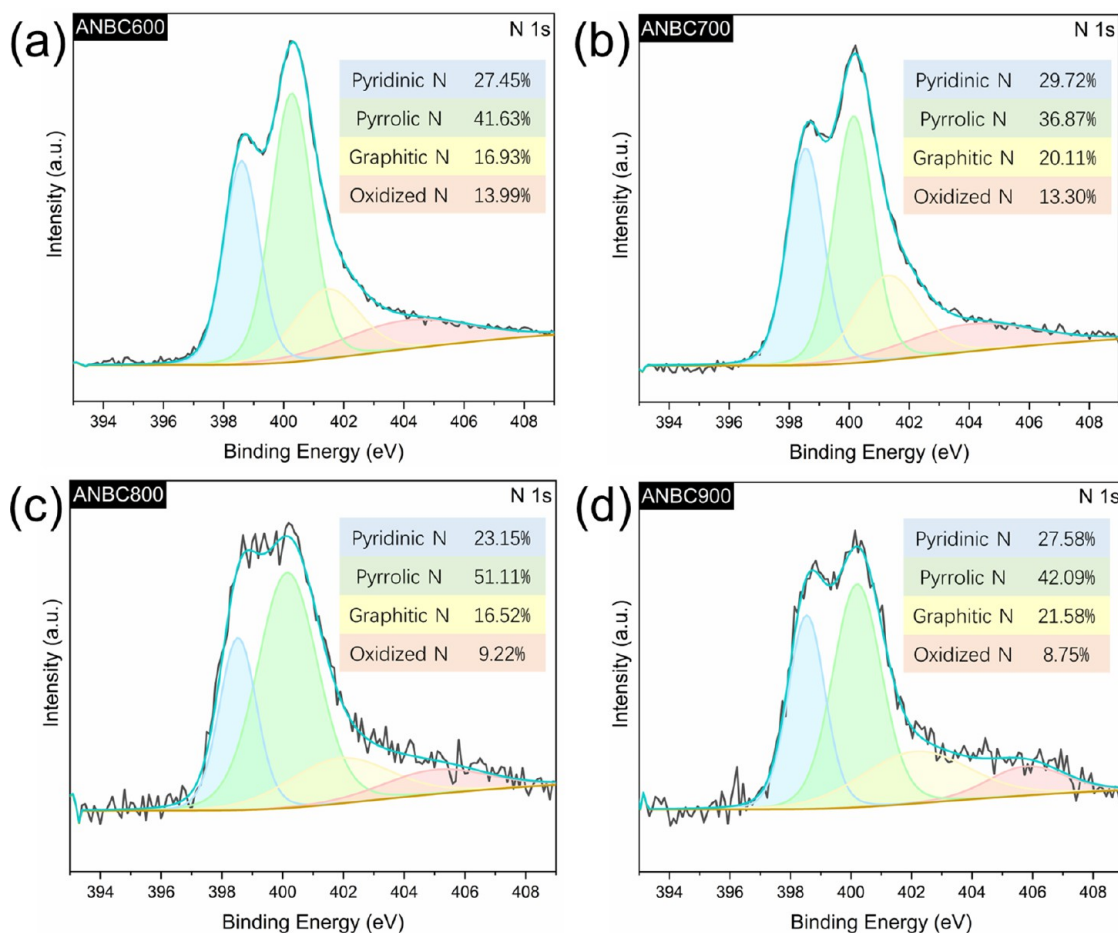
Figure 3. XPS high-resolution N 1s spectra of (a) ANBC600; (b) ANBC700; (c) ANBC800; and (d) ANBC900.

tion and leads to the removal of more heteroatoms. The high-resolution N 1s spectra of the ANBCT samples (Figure 3) are deconvoluted into four peaks at around 398.7, 400.3, 401.8, and 404.9 eV, corresponding to pyridinic N, pyrrolic N, graphitic N, and oxidized N configurations, respectively. With the increase in carbonization temperature, only the percentage of oxidized N showed a decreasing trend, while the percentage of pyridinic N, pyrrolic N, and graphitic N did not exhibit a clear trend. At all different carbonization temperatures, pyrrolic N is the main component, followed by pyridinic N and graphitic N. The high-resolution C 1s spectra of the ANBCT samples are shown in Figure S3. The C 1s can be resolved into three individual peaks at around 284.8, 285.7, and 288.0 eV, referring to C−C, C−N, and C−O, respectively.[42] The percentage of C−C (sp^2 carbon) from the deconvolution of high-resolution C 1s spectra is used as a descriptor to estimate the degree of graphitization of carbon materials.[43] The percentage of C−C (sp^2 carbon) shows an increasing trend with the increase in carbonization temperature, from 37.6% (ANBC600) to 46.7% (ANBC900), suggesting that the higher carbonization temperature induces a higher degree of graphitization of ANBCT samples.

To understand the hydrophilicity/hydrophobicity of the ANBCT samples, static contact angle measurements were carried out by the sessile drop method on the as-prepared electrode. The contact angle of fresh and used electrodes for each sample is depicted in Figure S4, and the data of each trial is summarized in Table S4. The contact angle increases with increasing carbonization temperature and gradually becomes stable. ANBC600 shows hydrophilicity, while the other samples show hydrophobicity, which can be explained by the removal of more hydrophilic O-containing and N-containing functional groups at higher carbonization temperatures, thus making the carbon surface more hydrophobic.[44] The comparison between fresh and used samples (after CO_2 electrochemical reduction) shows that the hydrophilicity/hydrophobicity characteristics of the N-doped biochar remained stable after 1 h CO_2 electrolysis.

Linear sweep voltammograms (LSV) were recorded in an Ar-saturated and CO_2-saturated 0.1 M aqueous $KHCO_3$ electrolyte at a scan rate of 5 mV/s to examine the electrochemical response of the ANBCT samples. As shown in Figure S5, all of the ANBCT samples exhibit a larger current density in the CO_2-saturated electrolyte than in the Ar-saturated electrolyte, suggesting that the biochars are active for the CO_2 reduction reaction. The voltammograms in a CO_2-saturated electrolyte are plotted in Figure 4a and show that all of the samples have a similar onset potential but reach different current densities in a potential window from −0.2 to −1.1 V vs RHE. Among them, ANBC600 shows a lower current density than other samples, which is attributed to its lower carbonization temperature. The lower degree of graphitization, smaller specific surface area, and less porosity jointly determine the poor electrochemical activity of ANBC600.

To further evaluate the catalytic performance of the ANBCT samples, chronoamperometry measurements were performed
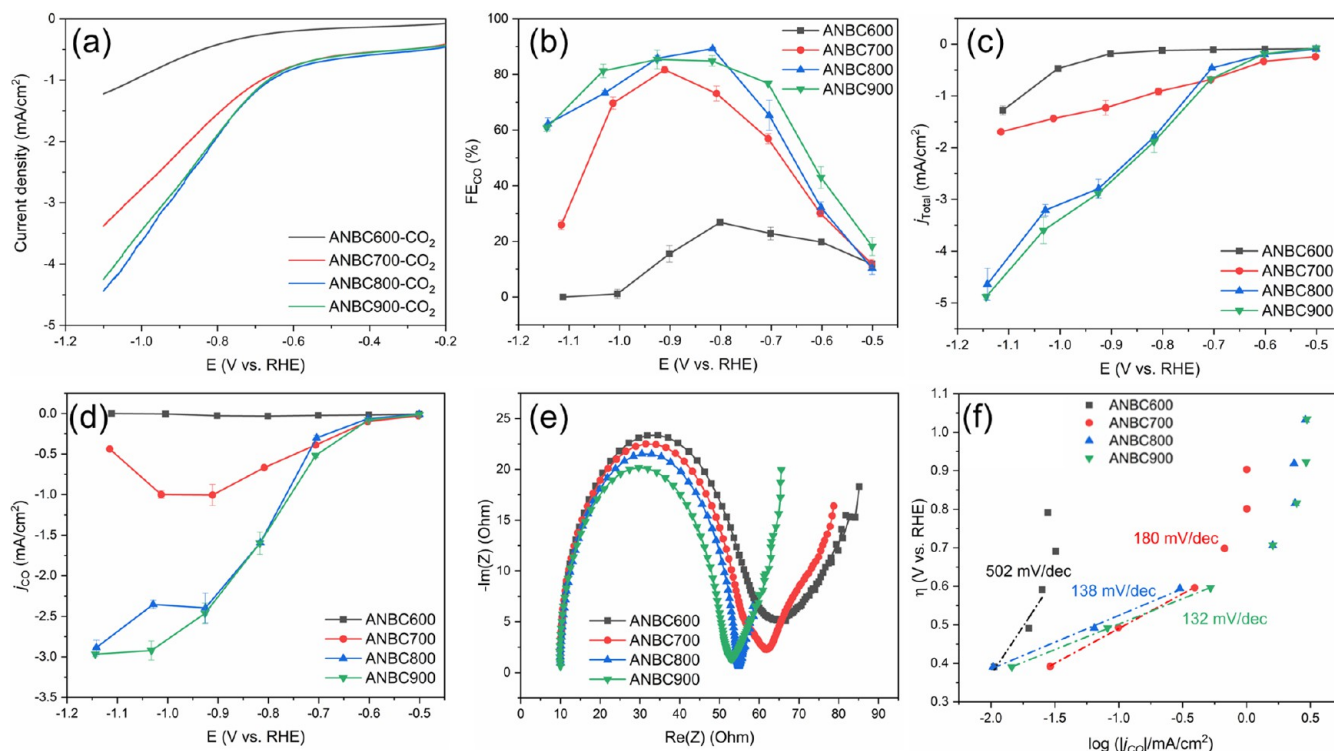
Figure 4. (a) LSV curves recorded in a CO_2-saturated 0.1 M KHCO$_3$ electrolyte; (b) FE of CO production at applied potentials from -0.5 to -1.15 V vs RHE; (c) total current density at different applied potentials; (d) partial current density of CO at different applied potentials; (e) Nyquist plots for the ANBCT samples; (f) Tafel plots of CO partial current density for the ANBCT samples in the CO_2-saturated 0.1 M KHCO$_3$ electrolyte.

for all samples at cathode potentials from -0.5 to -1.15 V vs RHE (with iR compensation, Figure S6). During these one-hour experiments, gaseous products were measured over two-minute intervals with an in-line gas chromatograph (GC), and aliquots of the electrolyte were injected into a high-performance liquid chromatograph (HPLC) to quantify liquid products. CO and H_2 were detected as the dominant gas products, while a trace amount of CH_4 (<1%) was detected at applied potentials more negative than -1 V vs RHE. No liquid products were detected by HPLC. The faradaic efficiencies (FE) of CO for the ANBCT samples are presented in Figure 4b, where the FE$_{CO}$ of all samples increased from -0.5 to -0.8 V vs RHE, reaching a maximum value at around -0.8 or -0.9 V vs RHE and then declining with the potential becoming more negative. This decline at higher applied potentials can be mainly attributed to the competition with the hydrogen evolution reaction (HER).[45] Figure 4b clearly shows that the FE$_{CO}$ increases with increasing carbonization temperature, with ANBC800 exhibiting the highest FE$_{CO}$ (89.3%) of all samples at -0.82 V vs RHE. Interestingly, the FE$_{CO}$ shows a significant increase when the carbonization temperature is increased from 600 to 700 °C, while it only shows a slight increase when the carbonization temperature is increased from 700 to 900 °C. Similarly, the total current density (j_{Total}) increases with the increase of carbonization temperature (see Figure 4c). Both ANBC800 and ANBC900 show a high FE$_{CO}$ and the highest partial current density toward CO (j_{CO}), as shown in Figure 4d. Moreover, the j_{CO} curves show significant differences in catalytic activity, with ANBC600 showing almost no activity toward CO_2 reduction. Additionally, the FE$_{H_2}$ and j_{H_2} are presented in Figure S7, with the FE$_{H_2}$ showing an opposite

trend to that of FE$_{CO}$ and ANBC900 showing the lowest FE$_{H_2}$ values, indicating that it is least active toward the HER.

Electrochemical impedance spectroscopy (EIS) was used to evaluate the charge transfer resistance of all ANBCT samples (see Figure 4e). ANBC900 shows the lowest charge transfer resistance (R_{ct}) compared to other samples, suggesting faster charge transfer during the CO_2RR.[46] The CO_2RR kinetics for the ANBCT samples were determined by plotting the Tafel slopes using the j_{CO} (Figure 4f). ANBC900 shows a lower Tafel slope (~132 mV/dec) than other samples, implying faster kinetics for CO formation.[47] The electrochemically active surface areas (ECSA) of ANBCT samples were determined by the double layer capacitance (C_{dl}) from cyclic voltammetry measurements (see Figure S8). With the increase of carbonization temperature, the C_{dl} value increases from 1.07 to 2.06 mF and then decreases to 1.50 mF. The measured C_{dl} shows a clear correlation with the specific surface area of ANBCT samples determined with N_2 adsorption–desorption isothermal analyses. However, there is no clear correlation between the C_{dl} values and the N-doping content of the samples. Even though the C_{dl} of ANBC800 is higher than ANBC900, they still show similar performance for the CO_2RR. To further confirm that the detected CO originates from CO_2 reduction instead of from the decomposition of carbon catalysts, control tests were carried out with an Ar-saturated electrolyte at -0.8 V vs RHE. As shown in Figure S9, only H_2 was detected during the Ar-saturated electrolysis, proving that the CO was produced from CO_2.

The carbonization temperature has a crucial influence on the physicochemical properties of N-doped biochar catalysts, which further affects its electrochemical performance for the CO_2RR. In general, the N-doped biochar synthesized at higher
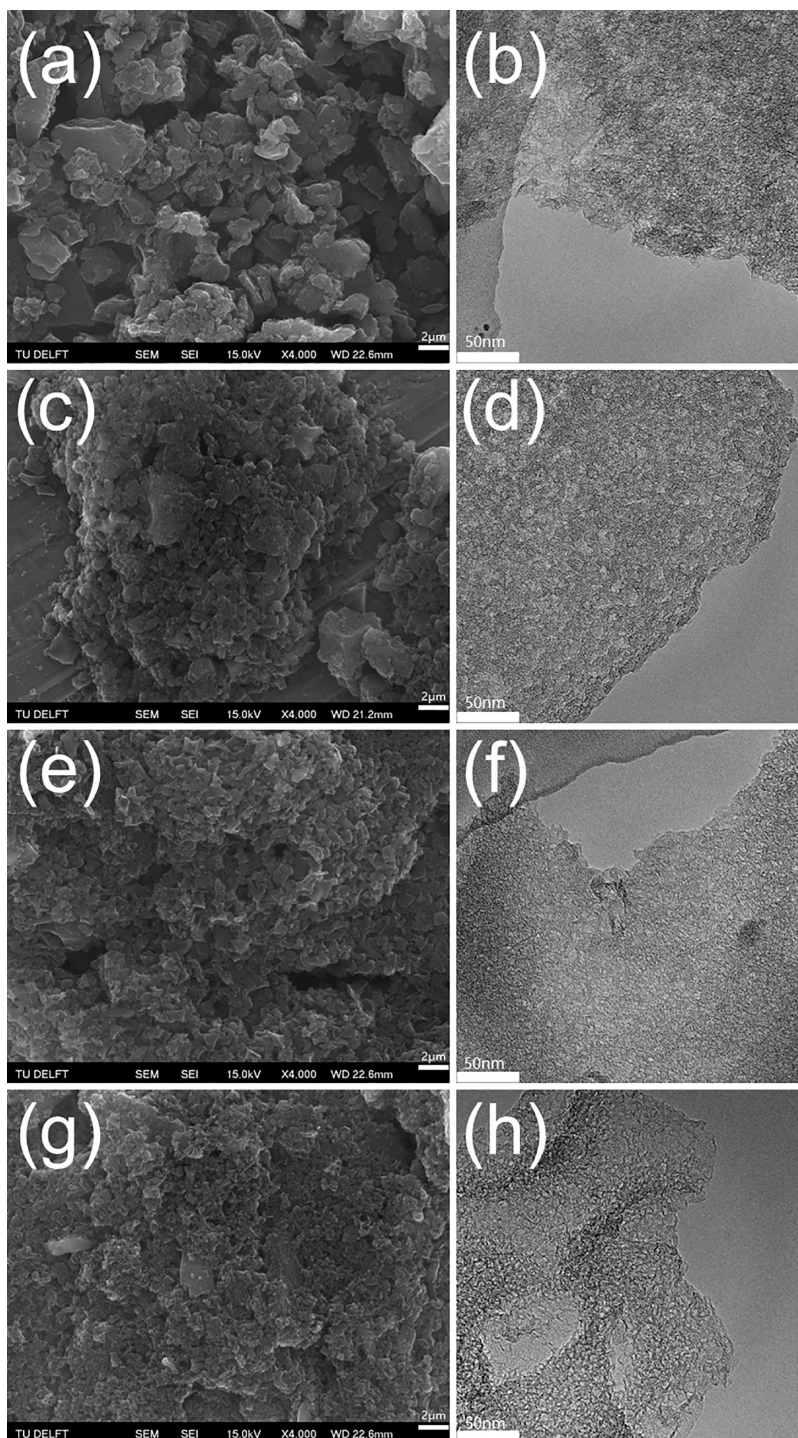
Figure 5. SEM (left) and TEM (right) images of ANBC800-SN: (a), (b); ANBC800-LN: (c), (d); ANBC800: (e), (f); and ANBC800-HN: (g), (h).

carbonization temperatures shows a better performance. In particular, ANBC800 and ANBC900 exhibit similar electrochemical performances, although they show significant differences in physicochemical properties, including N-doping content, specific surface area, porosity, the degree of graphitization, etc. We find that the CO_2RR performance of N-doped biochar is synergistically influenced by a multitude of physicochemical properties. For instance, the local environment surrounding the active sites has a critical impact on the expression of the electrocatalytic performance.[48] Our results show that the hydrophilicity/hydrophobicity of the N-doped biochar is strongly correlated with the FE_{CO}. Increasing the carbonization temperature leads to a higher hydrophobicity of the carbon catalysts, which enhances the FE_{CO} by inhibiting the HER. Moreover, the higher carbonization temperature leads to the removal of more heteroatoms, which improves the conductivity of the carbon catalysts. The higher carbonization temperature thereby causes smaller charge transfer resistances and results in faster CO_2 conversion kinetics to CO, which can
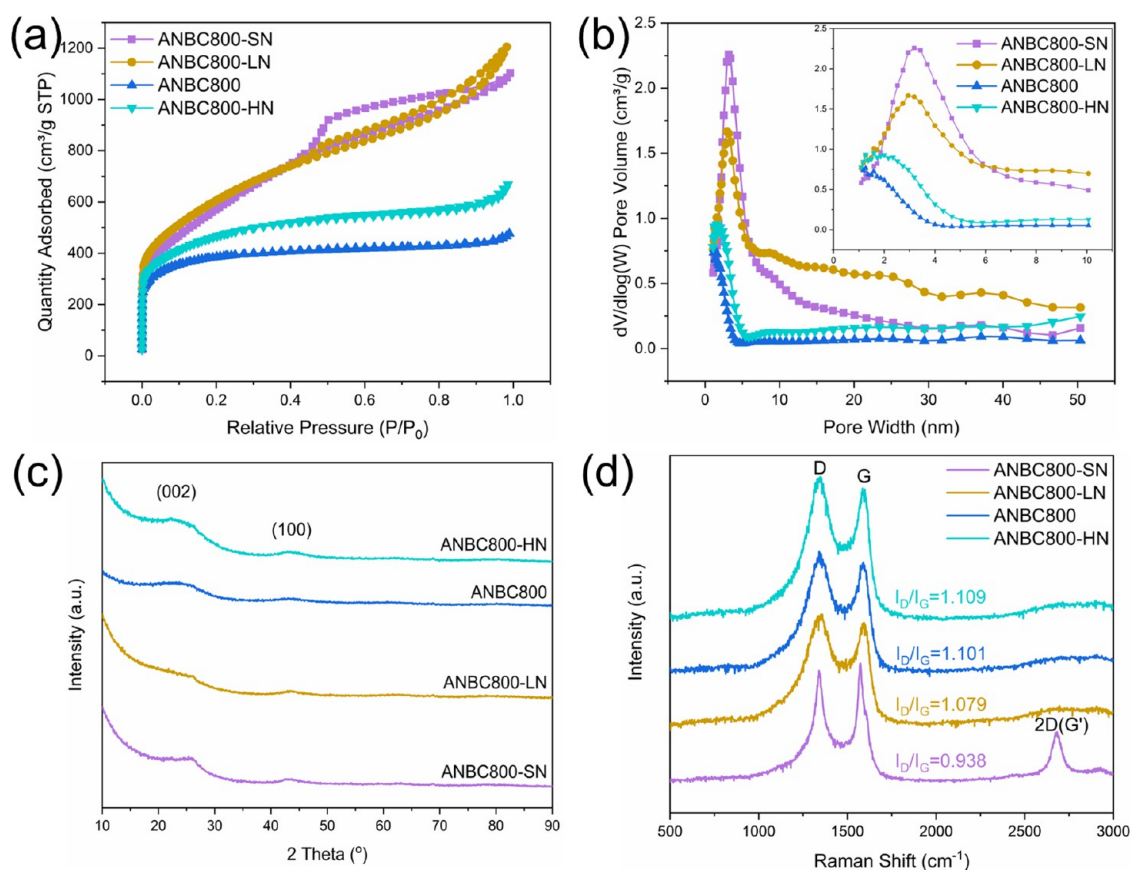
Figure 6. (a) N_2 adsorption–desorption isotherms; (b) pore size distribution; (c) XRD patterns; and (d) Raman spectra of the ANBC800-XN samples with different N-doping contents.

be considered as an important feature to improve the catalytic performance for the CO_2RR.

Effect of the N-Doping Level. To further investigate the effect of N-doping on the electrochemical performance of the CO_2RR, we synthesized a series of N-doped biochar catalysts with different amounts of N-doping by modifying the amount of urea added during the preparation processes. Taking into account the product selectivity and catalytic activity of the catalysts, ANBC800 was selected as a reference material as it exhibited high catalytic performance and had a higher carbon yield than ANBC900 (Table S1). The specific preparation procedure for the ANBC800-XN samples with modified N-doping amounts can be found in Table S1. The designation of the samples depends on the amount of urea addition. ANBC800-SN, ANBC800-LN, and ANBC800-HN imply that the ratio of bagasse to added urea to NaOH is 1: 0.5: 3, 1:1:3, and 1:3:3, respectively. The carbon yield increased from 1.6 wt % (ANBC800-SN) to 11.8 wt % (ANBC800-HN) with increasing urea addition. As the thermal decomposition of urea is an endothermic reaction, the lower amount of urea additions consumes less heat, which improves the biomass–activator interaction and results in a lower carbon yield. Conversely, a higher urea addition leads to more heat consumption during the pyrolysis, which weakens the interaction between the NaOH activator and the bagasse, resulting in a higher carbon yield.

The SEM and TEM images of the ANBC800-XN samples are depicted in Figure 5. SEM images show the morphology of the carbon samples, and the EDS images (Figure S10) show the elemental distribution. With low amounts of urea used

during synthesis, for example, with ANBC800-SN and ANBC800-LN, a larger bulk particle-stacked structure (Figure 5a,c) is observed. This effect is attributed to the stronger interaction between bagasse and NaOH, causing the collapse and shrinkage of the carbon materials, thus resulting in denser particles.[49] When the urea addition was higher, with ANBC800 and ANBC800-HN, a fluffier particle-stacked 3D structure is observed. The mesoporous structure of all ANBC800-XN samples can be clearly observed in the TEM images shown in Figure 5. Although the TEM images cannot quantify the size and proportion of mesopores, they illustrate that the mesoporous structures are effectively generated by the etching effect of the activator (ANBC800-SN and ANBC800-LN) and by gas–solid interaction reactions (ANBC800 and ANBC800-HN).

The mesoporosity of the samples is also reflected in the N_2 adsorption–desorption measurements. As shown in Figure 6a, ANBC800-SN and ANBC800-LN exhibit a clear hysteresis loop at relative pressures from 0.45 to 0.95, indicating that a large number of mesopores were created. For ANBC800 and ANBC800-HN, this hysteresis loop is almost negligible, suggesting a lower percentage of mesopores. Figure 6b displays the pore size distribution of the ANBC800-XN samples, which was calculated by a DFT model. ANBC800-SN and ANBC800-LN show a broad pore size distribution, and the peak is mainly centered at around 3 nm. However, ANBC800 and ANBC800-LN show a relatively narrow pore size distribution, and the pore size is concentrated at around 2 nm. The textural properties of the ANBC800-XN samples are summarized in Table S2. Both ANBC800-SN and ANBC800-
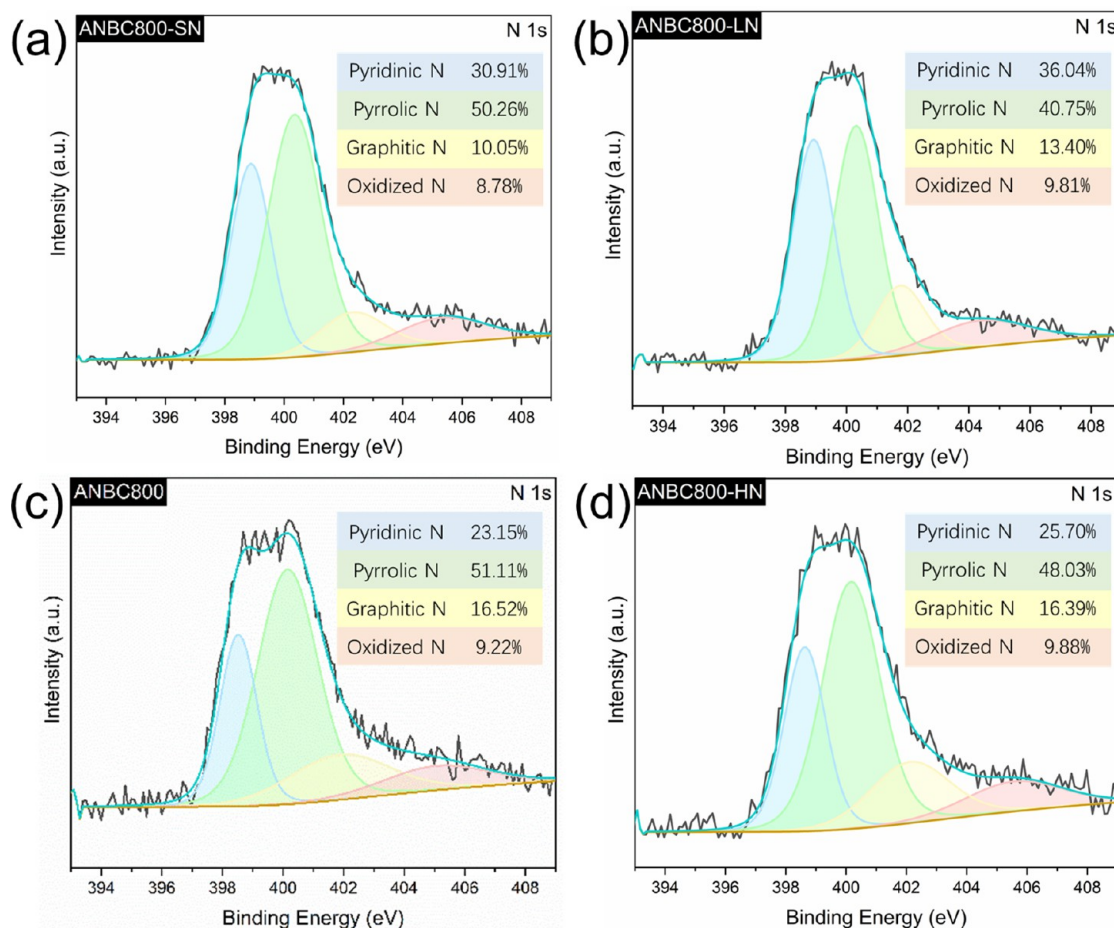
Figure 7. High-resolution N 1s spectrum of (a) ANBC800-SN; (b) ANBC800-LN; (c) ANBC800; and (d) ANBC800-HN.

LN display a large specific surface area (>2100 m^2/g) and larger ratio of mesopores (75.3 and 66.2%, respectively), which is mainly ascribed to the adequate reactions between bagasse and NaOH. By contrast, ANBC800 only has a specific surface area of 1426.9 m^2/g and less than 20% mesopores. The specific surface area, total pore volume, and ratio of mesopores for ANBC800-HN increased slightly compared to ANBC800. Despite the higher amount of urea added, leading to a higher heat consumption resulting in weaker biomass−activator interactions, the large amount of NH$_3$ released from urea decomposition etches the carbon skeleton, thereby increasing the specific surface area and total pore volume of the catalyst with respect to ANBC800.[36,50] Thus, the effect of the added amount of urea and the effect of the added activator jointly influences the development of porosity of N-doped biochar. The XRD patterns of all of the ANBC800-XN samples show coinciding characteristic peaks of the (002) and (100) planes of graphite (Figure 6c). The (002) peak reflection of ANBC800-SN and ANBC800-LN shifts to around 26°, indicating a higher degree of graphitization than for the other samples. Similar conclusions can also be drawn from the Raman spectra depicted in Figure 6d, where ANBC800-SN shows a lower I_D/I_G value (0.938) than other samples and also shows a 2D band at around 2700 cm^{-1}, implying a higher degree of graphitization for ANBC800-SN. The I_D/I_G value increases from 0.938 to 1.109 with the increase in urea addition since more urea will bring about more defects due to the etching of the carbon skeleton by NH$_3$.[45] Therefore,

although the carbonization temperature is the same, the different urea additions affect the structural properties of the carbon materials.

The full survey spectra of all of the ANBC800-XN samples in Figure S11 reveal the presence of C, N, and O on the carbon surface, and no other elements were detected. As shown in Table S3, the atomic concentration of N on the carbon surface increased gradually from 3.19 at % (ANBC800-SN) to 3.49 at % (ANBC800-LN) and further to 3.73 at % (ANBC800) and 4.19 at % (ANBC800-HN) with the increase of employed urea addition, but the concentration of C and O did not show an apparent trend with the changing of urea addition. In Figure 7, the high-resolution N 1s spectra of the ANBC800-XN samples are fitted into four individual peaks corresponding to pyridinic N, pyrrolic N, graphitic N, and oxidized N. At the same carbonization temperature, the increase in the total N-doping level did not have a significant effect on the distribution of different N-containing species. Pyrrolic N is still the main component, followed by pyridinic N, graphitic N, and oxidized N species. The high-resolution C 1s spectra of the ANBC800-XN samples are deconvoluted into three peaks, as shown in Figure S12, referring to C−C, C−N, and C−O.[42] All of the ANBC800-XN samples show a similar percentage of C−C (sp^2) carbon (40.5−46.5%), suggesting that modulating the N-doping level has a limited effect on the degree of graphitization of N-doped biochar at the same carbonization temperature.

The surface hydrophobicity measurements of the ANBC800-XN samples were carried out by static contact
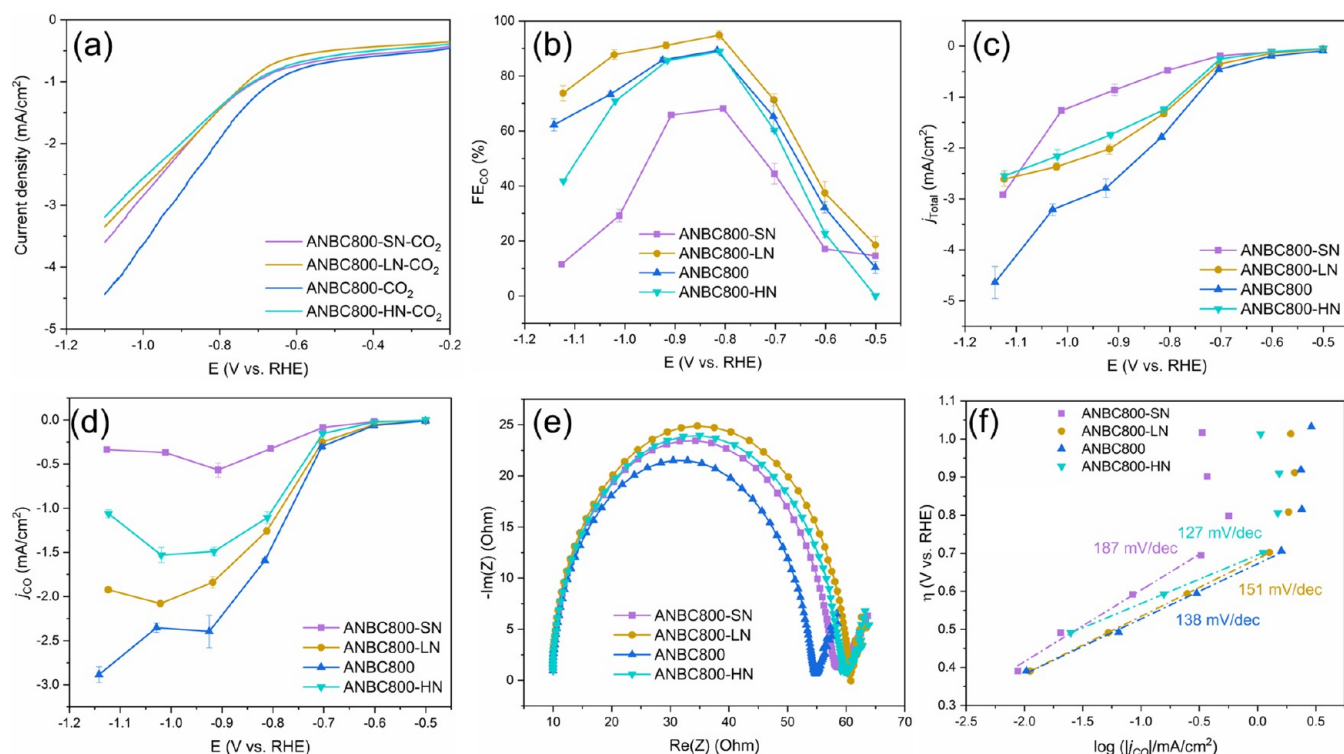
Figure 8. (a) LSV curves recorded in a CO_2-saturated 0.1 M $KHCO_3$ electrolyte; (b) FE of CO production at applied potentials from −0.5 to −1.15 V vs RHE; (c) total current density at different applied potentials; (d) partial current density of CO at different applied potentials; (e) Nyquist plots for the ANBC800-XN samples; (f) Tafel plots of CO partial current density for the ANBC800-XN samples in the CO_2-saturated 0.1 M $KHCO_3$ electrolyte.

angle tests. As shown in Figure S13, due to the same carbonization temperature, all catalysts showed similar hydrophobicity on the surface. With the increase of N-doping, the increase of N-containing functional groups on the surface can improve the surface wettability of porous carbon materials, resulting in a slight decrease of surface hydrophobicity.[51] The comparison of the contact angle of the fresh and used electrodes also shows that the hydrophobicity of the drop-cast catalysts is stable.

The LSV tests in Ar-saturated and CO_2-saturated 0.1 M $KHCO_3$ electrolytes are shown in Figure S14. ANBC800-SN shows almost the same catalytic activity in the Ar-saturated and CO_2-saturated electrolytes. ANBC800-LN and ANBC800-HN exhibit a slightly improved current density in a CO_2-saturated electrolyte with respect to the Ar-saturated electrolyte. However, this difference in current density diminishes as the potential becomes more negative, and even the ANBC800-HN displays a smaller current in a CO_2-saturated electrolyte than the Ar-saturated electrolyte at −1.0 to −1.1 V vs RHE. Only ANBC800 maintains better CO_2RR activity at −0.2 to −1.1 V vs RHE. According to the comparison from Figure 8a, ANBC800 shows higher current density in CO_2-saturated electrolysis than the other samples. The onset potential is similar for each sample. The chronoamperometry results are depicted in Figure S15, and the FE_{CO} of all samples are presented in Figure 8b, where ANBC800-SN, with the lowest N-doping level (3.19 at %), shows a relatively poor FE toward CO (68.2%). When the N-doping content was raised to 3.49 at %, the FE_{CO} of ANBC800-LN showed a better FE_{CO} at all potentials than the other samples, reaching a FE_{CO} of 94.9% at −0.82 V vs RHE. When the N-doping is further increased to 3.73 at % for ANBC800 and 4.19 at % for ANBC800-HN, the

FE_{CO} is slightly reduced. ANBC800 shows a higher total current density than other samples, as shown in Figure 8c. Although ANBC800 shows a slightly lower FE_{CO} than ANBC800-LN, it maintains a larger partial current density toward CO than the other samples due to its higher activity (see Figure 8d). The FE_{H2} and j_{H2} are presented in Figure S16 and show that ANBC800-SN exhibits higher activity toward HER at more negative potentials. The obtained results illustrate that the product selectivity to CO and catalytic activity of the catalysts are not consistently enhanced by increasing the amount of N-doping. Taking into account the charge transfer resistance of the catalysts, as shown in Figure 8e, ANBC800 exhibits smaller resistance than other samples, indicating that the charge transfer is more rapid than other samples. The Tafel plots are depicted in Figure 8f, with ANBC800-SN, ANBC800-LN, ANBC800, and ANBC800-HN displaying Tafel slopes of 187, 151, 138, and 127 mV/dec, respectively. All Tafel slopes are close to the theoretical value of 118 mV/dec (except for ANBC800-SN), suggesting that the rate-determining step of the CO_2RR for these samples is the single electron transfer to the adsorbed CO_2 to generate $*CO_2^-$ intermediates.[26,52] The ECSA measurement results of the ANBC800-XN samples are shown in Figure S17. Although ANBC800 and ANBC800-HN exhibit smaller specific surface area than ANBC800-SN and ANBC800-LN, their C_{dl} is higher than ANBC800-SN and ANBC800-LN, which is attributed to the higher percentage of micropores in these samples.[53] On the contrary, the larger pore sizes of ANBC800-SN and ANBC800-LN lead to a lower capacitance.[54] The C_{dl} of all samples does not show a clear correlation with the catalytic performances, indicating that not all of the electrochemically active sites show catalytic activity to the CO_2RR. The results of
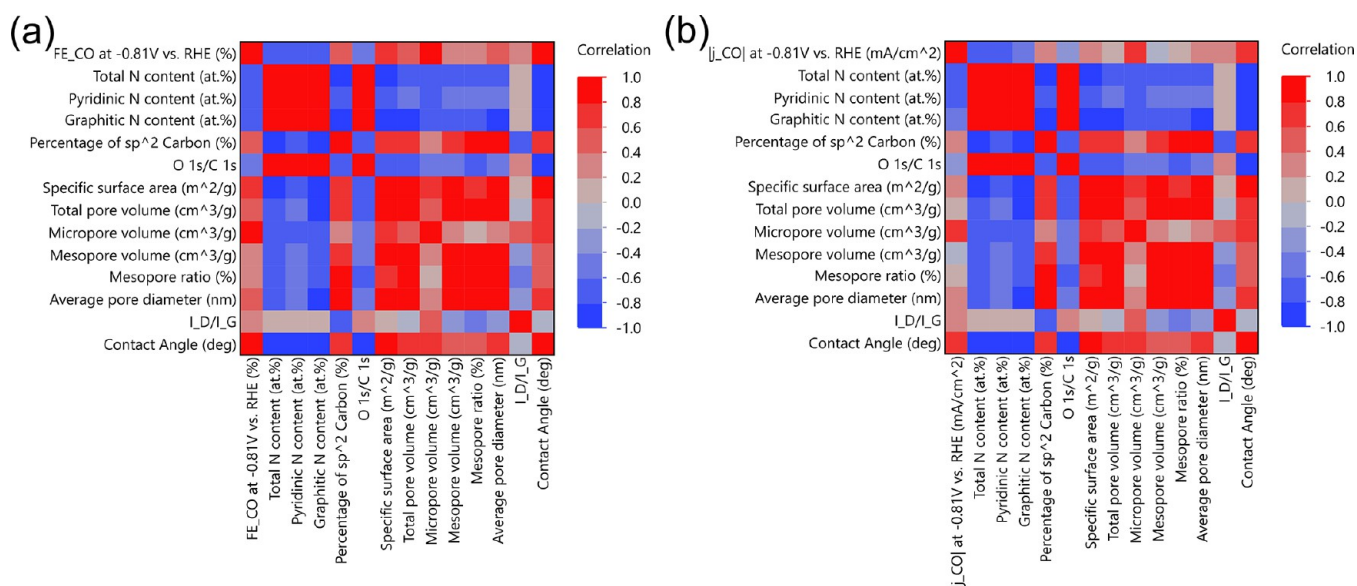
Figure 9. Heat maps indicating Pearson correlation between (a) FE_{CO} at -0.81 V vs RHE and different physicochemical properties; (b) $|j_{CO}|$ at -0.81 V vs RHE and different physicochemical properties.

control tests in Figure S18 confirm that CO_2 is the only carbon source for CO production.

In summary, we synthesized ANBC800-XN samples with different N-doping levels by adjusting the amount of urea addition during the preparation process and analyzed their physicochemical properties and electrochemical performance. Although all samples were prepared at the same carbonization temperature, the interaction between bagasse, urea, and NaOH was affected by the different amounts of urea addition, which changed the N-doping level, and also showed a significant effect on the pore structures of the catalysts. Among the synthesized samples, ANBC800-SN and ANBC800-LN exhibit an impressively large specific surface area (>2100 m^2/g) and a high ratio of mesopores ($>60\%$) but a relatively low N-doping level of 3.19 and 3.49 at %, respectively. ANBC800 and ANBC800-HN show a relatively lower specific surface area and the ratio of mesopores but a higher N-doping level of 3.73 and 4.19 at %, respectively. We demonstrate that neither the N-doping level nor the specific surface area is positively correlated to the observed CO_2RR performance of N-doped biochar catalysts, which is consistent with other literature findings.[28] Although ANBC800-SN and ANBC800-LN show a similar specific surface area and N-doping content, ANBC800-SN does not show a similar CO_2RR performance as ANBC800-LN. This is probably due to the excessive percentage of mesopores of ANBC800-SN (75.3%) that is not favorable for the adsorption of reactants and intermediates on the carbon surface, resulting in a lower FE and current density toward CO. Therefore, the contribution of micropores should not be underestimated. For example, Estevez et al. found that a higher microporous content can enhance CO_2 capture performance.[55] Additionally, Liu et al. reported a coal-based N-doped carbon catalyst for the CO_2RR and emphasized that the spatial confinement effect of the micropores can help CO_2 convert to CO efficiently.[20] Therefore, we hypothesize that a rational adjustment of the porosity of the catalyst, namely, the trade-off between mesopores and micropores structures, is crucial for the synthesis of superior CO_2RR electrocatalysts.

Understanding the Correlation between Physicochemical Properties and Electrochemical Performance.

As discussed above, the surface chemistry, the porous structure, the abundance of defects, the degree of graphitization, and the surface hydrophobicity of N-doped carbon catalysts all have a critical impact on their catalytic performance. Therefore, the overall performance of the catalysts for the CO_2RR cannot simply be reflected by one or two indicators. Therefore, a multivariate correlation analysis that combines the electrochemical performance and physicochemical properties of the N-doped biochar catalysts was carried out. The electrochemical performances of all samples were represented by the FE_{CO} and j_{CO} at around -0.81 V vs RHE, where most of the catalysts show their maximum FE to CO. The physicochemical properties were represented by the performed characterization of the surface chemical composition (the total N content, amount of pyridinic N, graphitic N, the percentage of sp^2 carbon, and the ratio of O 1s/C 1s from XPS), the pore structure (the specific surface area, total pore volume, micropore volume, mesopore volume, mesopore ratio, and average pore size from N$_2$ adsorption–desorption), the abundance of defects and the degree of graphitization (I_D/I_G ratio from Raman spectroscopy), and the surface hydrophobicity (contact angle measurements). JMP software was employed to perform the multivariate correlation analysis.[56] The resulting heat maps in Figure 9, which use Pearson correlation coefficients, were generated to visualize the correlation between pairs of variables. The red color indicates that the correlation coefficient is close to 1, suggesting a positive correlation, the blue color indicates that the correlation coefficient is close to -1, referring to a negative correlation, and the light gray color indicates that the coefficient is close to 0, implying that there is no correlation. More detailed multivariate scatterplots can be found in Figures S19 and S20.

As shown in Figure 9a,b, the heat maps reveal a negative correlation between the surface N-doping content and the FE_{CO} and j_{CO}. Furthermore, both pyridinic N and graphitic N show a negative correlation with the electrochemical performance of the CO_2RR. This negative correlation does not mean that less N-doping will result in better catalytic performance; it, however, does show that increasing the N-doping content is

not an effective way to improve the catalytic performance for the CO_2RR. The percentage of sp^2 carbon positively correlates with the FE_{CO} and j_{CO}, indicating that improving the degree of graphitization is helpful for the CO_2RR performance on N-doped carbon catalysts. The ratio of O 1s/C 1s shows a negative correlation with the FE_{CO} and j_{CO}, suggesting that the O-containing functional groups on the carbon surface hinder the catalytic performance. Interestingly, the porous structural properties of the catalysts show a positive correlation with the FE_{CO} (Figure 9a), indicating that increasing the specific surface area, micropore volume, and average pore size of the catalyst is an effective way to improve the product selectivity of the catalyst. However, the properties of these porous structures (except micropore volume) have almost no correlation with the partial current density of CO (Figure 9b). The abundance of defects (the I_D/I_G value) on the carbon surface shows a weak positive correlation with both the FE_{CO} and j_{CO}. The surface hydrophobicity also exhibits a positive correlation with both the FE_{CO} and j_{CO}, which indicates that this is an important parameter that significantly affects the CO_2RR performance.

Although the multivariate correlation analysis does not reveal the active sites for the CO_2RR on N-doped biochar, it highlights the importance of other physicochemical properties of N-doped biochar, which are usually overlooked. For instance, enhancing the degree of graphitization of N-doped carbon is helpful in improving the electrical conductivity, leading to improvement in the current densities of N-doped biochar catalysts. However, the graphitization process also promotes structural alignment by removing heteroatoms and defects, leading to the removal of active sites on N-doped carbon and a subsequent decrease in the product selectivity for the CO_2RR. On the other hand, the hydrophobicity of the N-doped biochar catalysts is improved with the increase of the degree of graphitization by removing the O-containing and N-containing functional groups. The higher hydrophobicity can improve the CO_2RR performance by suppressing the competitive HER. Furthermore, modulating the porosity, especially the percentage of mesopores of N-doped biochar, is helpful to improve the CO_2 transport within the catalyst, which also promotes the CO_2RR performance.

In addition, some interesting correlations between different physicochemical properties are observed. For instance, the N-containing and O-containing species on the carbon surface show a negative correlation to the structural properties of the N-doped biochar catalysts. This is due to the enhancement of the porous structure during the carbonization process, which is inevitably accompanied by the removal of heteroatoms. The surface hydrophobicity also shows a negative correlation to the surface heteroatom content, indicating that either N-containing species or O-containing species will reduce the hydrophobicity of the catalyst surface. However, surface hydrophobicity shows a positive correlation with porous structural properties.

Through the multivariate correlation analysis, we show a comprehensive analysis of the relationship between physicochemical properties and electrochemical performance. Although the limited number of samples cannot perfectly describe the correlation between the physicochemical properties and the electrochemical performance, our analysis is a useful guide for the design of N-doped carbon catalysts for the CO_2RR. Our results indicate that simply enlarging the specific surface area and increasing the N-doping level of N-doped

biochar catalysts is not an effective way to improve the CO_2RR performance. However, improving the surface hydrophobicity, the abundance of defects, and optimizing the porosity distribution of N-doped carbon can significantly improve the overall catalytic performance for CO_2 electrochemical reduction. It is important to note that the synergistic effect of various physicochemical properties, including N-doping content, specific surface area, porosity, degree of graphitization, the abundance of defects, and hydrophobicity, jointly determine the CO_2RR performance of N-doped biochar catalysts. Therefore, successfully revealing the structure—activity relationship of N-doped carbon catalysts for the CO_2RR needs more systematic and comprehensive analyses.

◼ CONCLUSIONS

In this study, we prepared N-doped carbon materials with different physicochemical properties and analyzed their electrochemical performances by controlling different carbonization temperatures and urea additions. Electrochemical measurements demonstrate that the higher carbonization temperature helps the N-doped carbon exhibit better electrochemical performance for the CO_2RR, even with lower N-doping levels. ANBC800 achieves 89.3% faradaic efficiency to CO with a CO partial current density of -1.59 mA/cm^2 at -0.82 V vs RHE. However, increasing the amount of N-doping did not effectively improve the performance of the catalysts for the CO_2RR. Adjusting the urea addition during the preparation process not only results in different amounts of N-doping but also dramatically changes the structural properties of the carbon material. In spite of showing a specific surface area larger than 2100 m^2/g, ANBC800-SN does not exhibit superb catalytic performance for the CO_2RR. In contrast, ANBC800-LN shows a similar specific surface area as ANBC800-SN but with a higher N-doping, and it exhibits 94.9% FE to CO at -0.82 V vs RHE. However, its lower catalytic activity leads to a lower partial current density for CO than ANBC800. These results further suggest that the CO_2RR performance of N-doped biochar is dependent on the synergistic effect of different physicochemical properties. The contribution of N-doping and specific surface area should, therefore, not be overemphasized. Further, a statistical-based multivariate correlation analysis visualizes the correlation between physicochemical properties and the electrocatalytic performances of the carbon materials prepared in this study. The N-doping content shows a negative correlation with the CO_2RR performance. The porous structural properties show a positive correlation to the FE_{CO} but almost no correlation to the j_{CO}. Therefore, tailoring the local environment of the N-doped carbon catalysts, such as the degree of graphitization, surface hydrophobicity, and the abundance of defects, is crucial for optimizing the electrocatalytic performance of N-doped carbon catalysts in the CO_2RR. Our data highlights the importance of a comprehensive analysis of the physicochemical properties of N-doped carbon catalysts for CO_2RR performance and enables the rational design of high-performance N-doped carbon catalysts for the CO_2RR in the future.

◼ ASSOCIATED CONTENT

ⓈI Supporting Information

The Supporting Information is available free of charge at https://pubs.acs.org/doi/10.1021/acscatal.3c01773.

Sample preparation summary; characterization results (SEM-EDS, N_2 adsorption−desorption, XPS, Contact angle); electrochemical measurement results (LSV, FE, and partial current density of H_2, CV for double layer capacitance, control experiment); and scatter plot matrix for the multivariant correlation analysis (PDF)

AUTHOR INFORMATION

Corresponding Author
Ruud Kortlever − *Large-Scale Energy Storage, Process & Energy Department, Faculty of Mechanical, Maritime and Materials Engineering, Delft University of Technology, 2628 CB Delft, The Netherlands;* orcid.org/0000-0001-9412-7480; Email: r.kortlever@tudelft.nl

Authors
Shilong Fu − *Large-Scale Energy Storage, Process & Energy Department, Faculty of Mechanical, Maritime and Materials Engineering, Delft University of Technology, 2628 CB Delft, The Netherlands*

Ming Li − *Large-Scale Energy Storage, Process & Energy Department, Faculty of Mechanical, Maritime and Materials Engineering, Delft University of Technology, 2628 CB Delft, The Netherlands; Product and Process Engineering, Chemical Engineering Department, Faculty of Applied Sciences, Delft University of Technology, 2628 HZ Delft, The Netherlands*

Wiebren de Jong − *Large-Scale Energy Storage, Process & Energy Department, Faculty of Mechanical, Maritime and Materials Engineering, Delft University of Technology, 2628 CB Delft, The Netherlands*

Complete contact information is available at:
https://pubs.acs.org/10.1021/acscatal.3c01773

Notes
The authors declare no competing financial interest.

REFERENCES

(1) Chu, S.; Majumdar, A. Opportunities and Challenges for a Sustainable Energy Future. *Nature* 2012, 488, 294−303.
(2) Saravanan, A.; Senthil kumar, P.; Vo, D.-V. N.; Vo, D. V.; Jeevanantham, S.; Jeevanantham, S.; Bhuvaneswari, V.; Bhuvaneswari, V.; Narayanan, V. A.; Anantha Narayanan, V.; Yaashikaa, P. R.; Yaashikaa, P.; Swetha, S.; Swetha, S.; Reshma, B. A Comprehensive Review on Different Approaches for CO2 Utilization and Conversion Pathways. *Chem. Eng. Sci.* 2021, 236, No. 116515.
(3) Seh, Z. W.; Kibsgaard, J.; Dickens, C. F.; Chorkendorff, I. B.; Nørskov, J. K.; Jaramillo, T. F. Combining Theory and Experiment in Electrocatalysis: Insights into Materials Design. *Science* 2017, 355, No. eaad4998.
(4) Peter, S. C. Reduction of CO2 to Chemicals and Fuels: A Solution to Global Warming and Energy Crisis. *ACS Energy Lett.* 2018, 3, 1557−1561.
(5) Kortlever, R.; Shen, J.; Schouten, K. J. P.; Calle-Vallejo, F.; Koper, M. T. M. Catalysts and Reaction Pathways for the Electrochemical Reduction of Carbon Dioxide. *J. Phys. Chem. Lett.* 2015, 6, 4073−4082.
(6) Pan, F.; Yang, Y. Designing CO 2 Reduction Electrode Materials by Morphology and Interface Engineering. *Energy Environ. Sci.* 2020, 13, 2275−2309.
(7) Lawrence, K. R.; Kumar, A. S.; Asperti, S.; van den Berg, D.; Girichandran, N.; Kortlever, R. Advances in Electrochemical Carbon Dioxide Reduction Toward Multi-Carbon Products. In *Chemical Valorisation of Carbon Dioxide*, 2022; pp 388−412.
(8) Zheng, T.; Jiang, K.; Wang, H. Recent Advances in Electrochemical CO2-to-CO Conversion on Heterogeneous Catalysts. *Adv. Mater.* 2018, 30, No. 1802066.
(9) Chen, C.; Khosrowabadi Kotyk, J. F.; Sheehan, S. W. Progress toward Commercial Application of Electrochemical Carbon Dioxide Reduction. *Chem* 2018, 4, 2571−2586.
(10) Han, N.; Ding, P.; He, L.; Li, Y.; Li, Y. Promises of Main Group Metal−Based Nanostructured Materials for Electrochemical CO2 Reduction to Formate. *Adv. Energy Mater.* 2020, 10, No. 2070046.
(11) Zhao, S.; Jin, R.; Jin, R. Opportunities and Challenges in CO2 Reduction by Gold-and Silver-Based Electrocatalysts: From Bulk Metals to Nanoparticles and Atomically Precise Nanoclusters. *ACS Energy Lett.* 2018, 3, 452−462.
(12) Adegoke, K. A.; Maxakato, N. W. Electrochemical CO2 Conversion to Fuels on Metal-Free N-Doped Carbon-Based Materials: Functionalities, Mechanistic, and Technoeconomic Aspects. *Mater. Today Chem.* 2022, 24, No. 100838.
(13) Paul, R.; Zhu, L.; Chen, H.; Qu, J.; Dai, L. Recent Advances in Carbon-Based Metal-Free Electrocatalysts. *Adv. Mater.* 2019, 31, 1806403.
(14) Wu, J.; Yadav, R. M.; Liu, M.; Sharma, P. P.; Tiwary, C. S.; Ma, L.; Zou, X.; Zhou, X. D.; Yakobson, B. I.; Lou, J.; Ajayan, P. M. Achieving Highly Efficient, Selective, and Stable CO_2 Reduction on Nitrogen-Doped Carbon Nanotubes. *ACS Nano* 2015, 9, 5364−5371.
(15) Liu, S.; Yang, H.; Huang, X.; Liu, L.; Cai, W.; Gao, J.; Li, X.; Zhang, T.; Huang, Y.; Liu, B. Identifying Active Sites of Nitrogen-Doped Carbon Materials for the CO2 Reduction Reaction. *Adv. Funct. Mater.* 2018, 28, No. 1800499.
(16) Liu, Y.; Chen, S.; Quan, X.; Yu, H. Efficient Electrochemical Reduction of Carbon Dioxide to Acetate on Nitrogen-Doped Nanodiamond. *J. Am. Chem. Soc.* 2015, 137, 11631−11636.
(17) Hu, C.; Dai, L. Doping of Carbon Materials for Metal-Free Electrocatalysis. *Adv. Mater.* 2019, 31, 1804672.
(18) Li, F.; Xue, M.; Knowles, G. P.; Chen, L.; MacFarlane, D. R.; Zhang, J. Porous Nitrogen−Doped Carbon Derived from Biomass for Electrocatalytic Reduction of CO2 to CO. *Electrochim. Acta* 2017, 245, 561−568.
(19) Abdelkader-Fernández, V. K.; Fernandes, D. M.; Freire, C. Carbon-Based Electrocatalysts for CO2 Electroreduction Produced via MOF, Biomass, and Other Precursors Carbonization: A Review. *J. CO2 Util.* 2020, 42, No. 101350.
(20) Liu, W.; Qi, J.; Bai, P.; Zhang, W.; Xu, L. Utilizing Spatial Confinement Effect of N Atoms in Micropores of Coal-Based Metal-Free Material for Efficiently Electrochemical Reduction of Carbon Dioxide. *Appl. Catal., B* 2020, 272, No. 118974.
(21) Zhu, D. D.; Liu, J. L.; Qiao, S. Z. Recent Advances in Inorganic Heterogeneous Electrocatalysts for Reduction of Carbon Dioxide. *Adv. Mater.* 2016, 28, 3423−3452.
(22) Kuang, M.; Guan, A.; Gu, Z.; Han, P.; Qian, L.; Zheng, G. Enhanced N-Doping in Mesoporous Carbon for Efficient Electrocatalytic CO2 Conversion. *Nano Res.* 2019, 12, 2324−2329.
(23) Ma, C.; Hou, P.; Wang, X.; Wang, Z.; Li, W.; Kang, P. Carbon Nanotubes with Rich Pyridinic Nitrogen for Gas Phase CO2 Electroreduction. *Appl. Catal., B* 2019, 250, 347−354.
(24) Zhang, Z.; Yu, L.; Tu, Y.; Chen, R.; Wu, L.; Zhu, J.; Deng, D. Unveiling the Active Site of Metal-Free Nitrogen-Doped Carbon for Electrocatalytic Carbon Dioxide Reduction. *Cell Reports Phys. Sci.* 2020, 1, No. 100145.
(25) Cui, X.; Pan, Z.; Zhang, L.; Peng, H.; Zheng, G. Selective Etching of Nitrogen-Doped Carbon by Steam for Enhanced

Electrochemical CO 2 Reduction. *Adv. Energy Mater.* **2017**, *7*, 1701456.

(26) Li, H.; Xiao, N.; Hao, M.; Song, X.; Wang, Y.; Ji, Y.; Liu, C.; Li, C.; Guo, Z.; Zhang, F.; Qiu, J. Efficient CO2 Electroreduction over Pyridinic-N Active Sites Highly Exposed on Wrinkled Porous Carbon Nanosheets. *Chem. Eng. J.* **2018**, *351*, 613−621.

(27) Li, J.; Zan, W. Y.; Kang, H.; Dong, Z.; Zhang, X.; Lin, Y.; Mu, Y. W.; Zhang, F.; Zhang, X. M.; Gu, J. Graphitic-N Highly Doped Graphene-like Carbon: A Superior Metal-Free Catalyst for Efficient Reduction of CO2. *Appl. Catal., B* **2021**, *298*, No. 120510.

(28) Daiyan, R.; Tan, X.; Chen, R.; Saputera, W. H.; Tahini, H. A.; Lovell, E.; Ng, Y. H.; Smith, S. C.; Dai, L.; Lu, X.; Amal, R. Electroreduction of CO2 to CO on a Mesoporous Carbon Catalyst with Progressively Removed Nitrogen Moieties. *ACS Energy Lett.* **2018**, *3*, 2292−2298.

(29) Hursán, D.; Samu, A. A.; Janovák, L.; Artyushkova, K.; Asset, T.; Atanassov, P.; Janáky, C. Morphological Attributes Govern Carbon Dioxide Reduction on N-Doped Carbon Electrodes. *Joule* **2019**, *3*, 1719−1733.

(30) Fu, S.; Li, M.; Asperti, S.; De Jong, W.; Kortlever, R.; Fu, S.; Li, M.; Asperti, S.; De Jong, I. W.; Kortlever, R.; Li, M. Unravelling the Effect of Activators Used in the Synthesis of Biomass-Derived Carbon Electrocatalysts on the Electrocatalytic Performance for CO2 Reduction. *ChemSusChem* **2023**, *16*, e202202188.

(31) Liu, W. J.; Jiang, H.; Yu, H. Q. Development of Biochar-Based Functional Materials: Toward a Sustainable Platform Carbon Material. *Chem. Rev.* **2015**, *115*, 12251−12285.

(32) Liu, W.-J.; Jiang, H.; Yu, H.-Q. Emerging Applications of Biochar-Based Materials for Energy Storage and Conversion. *Energy Environ. Sci.* **2019**, *12*, 1751−1779.

(33) Lobaccaro, P.; Singh, M. R.; Clark, E. L.; Kwon, Y.; Bell, A. T.; Ager, J. W. Effects of Temperature and Gas−Liquid Mass Transfer on the Operation of Small Electrochemical Cells for the Quantitative Evaluation of CO 2 Reduction Electrocatalysts. *Phys. Chem. Chem. Phys.* **2016**, *18*, 26777−26785.

(34) Zhang, Y.; Song, X.; Xu, Y.; Shen, H.; Kong, X.; Xu, H. Utilization of Wheat Bran for Producing Activated Carbon with High Specific Surface Area via NaOH Activation Using Industrial Furnace. *J. Clean. Prod.* **2019**, *210*, 366−375.

(35) Lin, L.; Zhai, S.-R.; Xiao, Z.-Y.; Song, Y.; An, Q.-D.; Song, X.-W. Dye Adsorption of Mesoporous Activated Carbons Produced from NaOH-Pretreated Rice Husks. *Bioresour. Technol.* **2013**, *136*, 437−443.

(36) Zou, K.; Deng, Y.; Chen, J.; Qian, Y.; Yang, Y.; Li, Y.; Chen, G. Hierarchically Porous Nitrogen-Doped Carbon Derived from the Activation of Agriculture Waste by Potassium Hydroxide and Urea for High-Performance Supercapacitors. *J. Power Sources* **2018**, *378*, 579−588.

(37) Qiu, T.; Yang, J.-G.; Bai, X.-J.; Wang, Y.-L. The Preparation of Synthetic Graphite Materials with Hierarchical Pores from Lignite by One-Step Impregnation and Their Characterization as Dye Absorbents. *RSC Adv.* **2019**, *9*, 12737−12746.

(38) Vinayan, B. P.; Nagar, R.; Raman, V.; Rajalakshmi, N.; Dhathathreyan, K. S.; Ramaprabhu, S. Synthesis of Graphene-Multiwalled Carbon Nanotubes Hybrid Nanostructure by Strengthened Electrostatic Interaction and Its Lithium Ion Battery Application. *J. Mater. Chem.* **2012**, *22*, 9949−9956.

(39) Li, K.; Chen, W.; Yang, H.; Chen, Y.; Xia, S.; Xia, M.; Tu, X.; Chen, H. Mechanism of Biomass Activation and Ammonia Modification for Nitrogen-Doped Porous Carbon Materials. *Bioresour. Technol.* **2019**, *280*, 260−268.

(40) Niu, Q.; Gao, K.; Tang, Q.; Wang, L.; Han, L.; Fang, H.; Zhang, Y.; Wang, S.; Wang, L. Large-Size Graphene-like Porous Carbon Nanosheets with Controllable N-Doped Surface Derived from Sugarcane Bagasse Pith/Chitosan for High Performance Supercapacitors. *Carbon* **2017**, *123*, 290−298.

(41) Ayiania, M.; Smith, M.; Hensley, A. J. R.; Scudiero, L.; McEwen, J. S.; Garcia-Perez, M. Deconvoluting the XPS Spectra for Nitrogen-Doped Chars: An Analysis from First Principles. *Carbon* **2020**, *162*, 528−544.

(42) Li, X.; Guan, B. Y.; Gao, S.; Lou, X. W. A General Dual-Templating Approach to Biomass-Derived Hierarchically Porous Heteroatom-Doped Carbon Materials for Enhanced Electrocatalytic Oxygen Reduction. *Energy Environ. Sci.* **2019**, *12*, 648−655.

(43) Lin, Y.; Feng, Z.; Yu, L.; Gu, Q.; Wu, S.; Su, D. S. Insights into the Surface Chemistry and Electronic Properties of Sp2 and Sp3-Hybridized Nanocarbon Materials for Catalysis. *Chem. Commun.* **2017**, *53*, 4834−4837.

(44) Masoumi, S.; Dalai, A. K. Optimized Production and Characterization of Highly Porous Activated Carbon from Algal-Derived Hydrochar. *J. Clean. Prod.* **2020**, *263*, No. 121427.

(45) Li, C.; Wang, Y.; Xiao, N.; Li, H.; Ji, Y.; Guo, Z.; Liu, C.; Qiu, J. Nitrogen-Doped Porous Carbon from Coal for High Efficiency CO2 Electrocatalytic Reduction. *Carbon* **2019**, *151*, 46−52.

(46) Yao, P.; Qiu, Y.; Zhang, T.; Su, P.; Li, X.; Zhang, H. N-Doped Nanoporous Carbon from Biomass as a Highly Efficient Electrocatalyst for the CO2 Reduction Reaction. *ACS Sustainable Chem. Eng.* **2019**, *7*, 5249−5255.

(47) Ma, X.; Du, J.; Sun, H.; Ye, F.; Wang, X.; Xu, P.; Hu, C.; Zhang, L.; Liu, D. Boron, Nitrogen Co-Doped Carbon with Abundant Mesopores for Efficient CO2 Electroreduction. *Appl. Catal., B* **2021**, *298*, No. 120543.

(48) Wu, Q.; Gao, J.; Feng, J.; Liu, Q.; Zhou, Y.; Zhang, S.; Nie, M.; Liu, Y.; Zhao, J.; Liu, F.; Zhong, J.; Kang, Z. A CO 2 Adsorption Dominated Carbon Defect-Based Electrocatalyst for Efficient Carbon Dioxide Reduction. *J. Mater. Chem. A* **2020**, *8*, 1205−1211.

(49) Liu, W.; Qi, J.; Bai, P.; Zhang, W.; Xu, L. Utilizing Spatial Confinement Effect of N Atoms in Micropores of Coal-Based Metal-Free Material for Efficiently Electrochemical Reduction of Carbon Dioxide. *Appl. Catal., B* **2020**, *272*, No. 118974.

(50) Ning, H.; Guo, D.; Wang, X.; Tan, Z.; Wang, W.; Yang, Z.; Li, L.; Zhao, Q.; Hao, J.; Wu, M. Efficient CO2 Electroreduction over N-Doped Hieratically Porous Carbon Derived from Petroleum Pitch. *J. Energy Chem.* **2021**, *56*, 113−120.

(51) Gang, X.; Krishnamoorthy, M.; Jiang, W.; Pan, J.; Pan, Z.; Liu, X. A Novel In-Situ Preparation of N-Rich Spherical Porous Carbon as Greatly Enhanced Material for High-Performance Supercapacitors. *Carbon* **2021**, *171*, 62−71.

(52) Deng, W.; Zhang, P.; Seger, B.; Gong, J. Unraveling the Rate-Limiting Step of Two-Electron Transfer Electrochemical Reduction of Carbon Dioxide. *Nat. Commun.* **2022**, *13*, No. 803.

(53) Chmiola, J.; Yushin, G.; Gogotsi, Y.; Portet, C.; Simon, P.; Taberna, P.-L. Anomalous Increase in Carbon Capacitance at Pore Sizes Less than 1 Nanometer. *Science* **2006**, *313*, 1760−1763.

(54) Largeot, C.; Portet, C.; Chmiola, J.; Taberna, P.-L.; Gogotsi, Y.; Simon, P. Relation between the Ion Size and Pore Size for an Electric Double-Layer Capacitor. *J. Am. Chem. Soc.* **2008**, *130*, 2730−2731.

(55) Estevez, L.; Barpaga, D.; Zheng, J.; Sabale, S.; Patel, R. L.; Zhang, J. G.; McGrail, B. P.; Motkuri, R. K. Hierarchically Porous Carbon Materials for CO2 Capture: The Role of Pore Structure. *Ind. Eng. Chem. Res.* **2018**, *57*, 1262−1268.

(56) Oates, R. P.; Murawski, J.; Hor, C.; Shen, X.; Weber, D. J.; Oezaslan, M.; Shaffer, M. S. P.; Stephens, I. E. L. How to Minimise Hydrogen Evolution on Carbon Based Materials? *J. Electrochem. Soc.* **2022**, *169*, 054516.